Above-Threshold Ionisation with Two-Colour Laser Fields

Master's Thesis by Leon Petersson

LUNDS UNIVERSITET

Lund Reports on Atomic Physics, LRAP-499
December 2, 2014

Contents

Acknowledgements

I would like to thank all the members of the Attosecond Physics research group at LTH, for many interesting and enjoyable discussions, which have aided me greatly in my work. For the great help they have been, and the great insights they have provided, I would like to extend special thanks to Neven Ibrakovič, Hélène Coudert-Alteirac, Esben Witting Larsen and Diego Guénot.

Above all, I would like to express my gratitude to my two supervisors, Johan Mauritsson and Stefanos Carlström. Their ideas, and guidance have been vital to this thesis.

The Swedish National Infrastructure for Computing (SNIC) has aided me by providing valuable computing resources. For this I extend my thanks to their staff.

While writing this thesis, I have had very good time. I would like to thank everyone who has contributed to the enjoyable work atmosphere.

Populärvetenskaplig Sammanfattning

En atom består av en kärna och en eller flera elektroner. Den positivt laddade kärnan utgör atomens centrum och större delen av dess massa. Elektronerna är små, negativt laddade, partiklar i omloppsbana kring kärnan. För många applikationer (och inte minst för att studera atomstruktur) kan det vara interessant att kunna slita loss elektronerna ur sina banor – att jonisera atomen.

Ett sätt att jonisera en atom är att använda en laser. En laser genererar en stråle av ljus, vilka slänger elektronerna de passerar upp och ner, likt en boj som guppar i havet. Oftast är ljusvågorna symmetriska: hälften av tiden dras elektronerna åt ena hållet, och hälften av tiden dras de åt det andra.

Om lasern är tillräckligt kommer elektroner att dras loss från sina atomer och frigöras – atomerna joniseras. De fria elektronerna kommer att slungas fram och tillbaka av ljusvågorna tills de antingen lämnar laserstrålen eller slungas tillbaka in i atomen av vågorna. De som slungas tillbaka kommer antingen att falla in i atomen eller att studsa ut igen.

Laserljus består nästan alltid av endast en våglängd, vilket är ett mått på färgen hos det ljus som genereras. Vad händer om man istället för att använda en använder två laserstrålar med olika färg? I det här examensarbetet undersöks vad som händer om man använder två lasrar, en stark och en svag, där den svaga laserns vågor gungar flera gånger snabbare än den starkas.

En illustration av detta ses i figur 1 nedan, där en pensel har satts fast på varje hjul av en cykel. Eftersom den blå penseln på det lilla hjulet fullbordar en rotation dubbelt så ofta som den röda penseln på det stora hjulet, kommer vågen som målas av det lilla hjulet svänga dubbelt så snabbt. Man säger att det lilla hjulet har två gånger högre *frekvens* än det stora. Notera att en två gånger högre frekvens även leder till en hälften så lång våglängd.

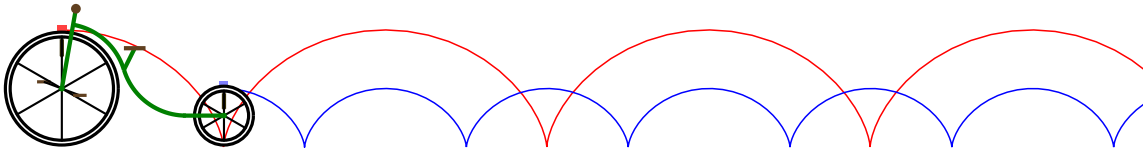

Figur 1: En röd och en blå pensel har satts fast på fram- respektive bakhjulet av en cykel målar en vägg. Det lilla hjulet roterar fler varv än det stora på samma tid, vilket illustreras av färgen på väggen.

När elektronerna är fria slängs de, som nämnt ovan, fram och tillbaka tills de lämnar laserstrålen. Deras acceleration är proportionell mot summan av laservågornas höjd. Här studerades endast fallet där fältet med högst frekvens är för svagt för att påverka accelerationen. Detta medför att elektronernas energi efter att de lämnar atomen inte påverkas av det svaga fältet i någon större utsträckning. Den högfrekventa lasern kan dock påverka sannolikheten för jonisation vid en viss tidpunkt, vilket illustreras i figur 2. Eftersom jon-

isationstillfället påverkar den frigjorda elektronens energi, påverar den högfrekventa lasern hur många elektroner som kommer uppmätas med en given energi.

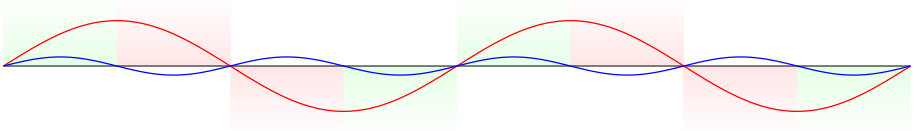

Figur 2: Två lasrar med olika frekvens interagerar. När båda pekar åt samma håll ökar jonisationssannolikheten, annars minskar den. Grön respektive röd färg representerar ökad respektive minskad jonisationssannolikhet.

Genom att observera sannolikheten för elektroner att ha olika energier, vet man sannolikheten för att de ska frigöras vid olika tidpunkter. Elektroner som frigörs när den starka lasern pekar uppåt åker uppåt och de som joniseras när den pekar neråt åker neråt. I de områden där jonisationen ökar hos de elektroner som åker uppåt (till exempel innan de positiva vågtopparna i figur 2), minskar den för de som åker neråt, och vice versa. Detta betyder att endast skillnaden mellan hur många elektroner som åker uppåt och nedåt med en viss energi behöver studeras. På detta sätt kan man få information om den relativa förskjutningen i tidled mellan vågorna, vilket ger en större förståelse för vad som händer i det fysiska systemet man studerar. Ett exempel på en annan relativ förskjutning ges i figur 3.

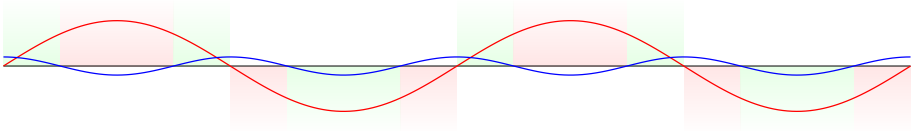

Figur 3: Vågor av samma frekvens och styrka som i figur 2, men med annan relativ förskutning.

När vågornas frekvens skiljer sig med en udda faktor, såsom i figur 4, kommer lasern att accelerera lika många elektroner med samma energi både uppåt och nedåt. I detta fall kan inte systemets asymmetri undersökas. Istället kan endast det totala antalet elektroner joniserade med en viss energi studeras.

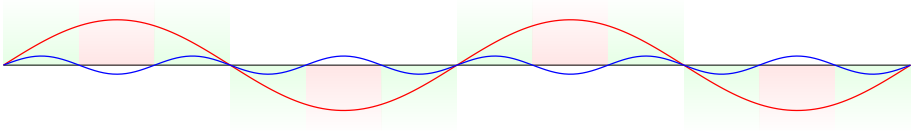

Figur 4: Vågor av samma förskjutning och styrka som i figur 2. Dock är här skillnaden i frekvens en faktor 3.

1 Introduction

When atoms are exposed to a strong laser field, their electrons can, using a quantum mechanical description, be seen as absorbing more photons than required for ionisation, a process known as Above Threshold Ionisation (ATI) [1]. If the probability for an electron freed during ATI to absorb at least one photon is p, the probability to absorb at least two will be p^2, three p^3, and so on. The energy of the electrons is proportional to the number of photons used to excite them, giving an exponentially decreasing number of observed electrons as a function of energy [2]. This process is illustrated in figure 1.

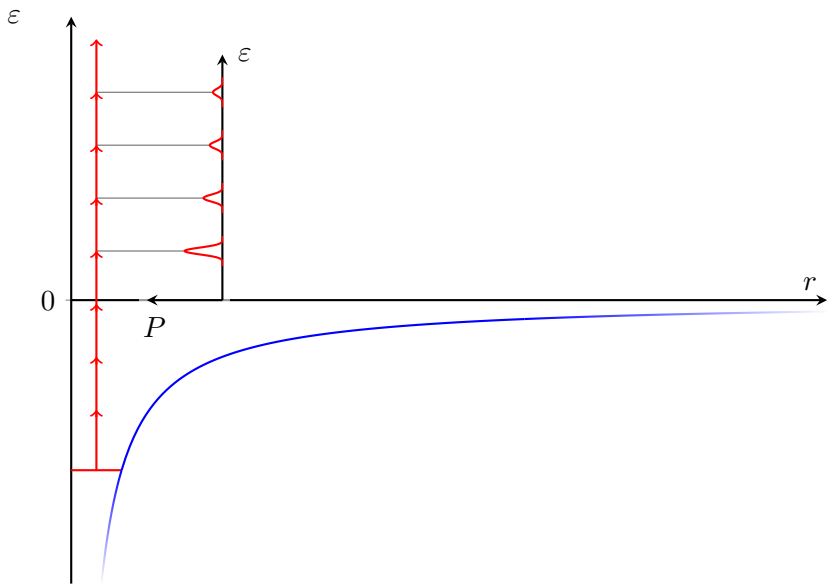

Figure 1: An illustration of ionisation during ATI. In the $r-\varepsilon$ plane, where r is the distance from the atomic core and ε is the energy, it is illustrated how an electron is freed from its ground state in an atomic potential using multiple photons. As can be seen in the $\varepsilon - P$ plane, where $P(\varepsilon)$ is the probability of finding an electron with energy ε, the exponentially decreasing pattern emerges.

According to the classical description of ATI, the electrons can be seen as gaining kinetic energy due to their time in the electromagnetic field from the laser. The force $\vec{F}$ exerted on the electrons with charge q is

$$\vec{F} = q\left[\vec{E}(t) + \vec{v} \times \vec{B}(t)\right], \tag{1}$$

where $\vec{E}$ is the electric field, and $\vec{B}$ the magnetic field.

The strength of the magnetic field can be written

$$|\vec{B}| = \frac{|\vec{E}|}{c}, \tag{2}$$

where c is the speed of light. For non-relativistic velocities $\vec{v}$, this implies that the force due to the magnetic field can be neglected and the force approximated as

$$\vec{F}(t) \approx q\vec{E}(t). \tag{3}$$

Consider a linearly polarised laser. If the electron has mass m_e, and the distance x from the atom, its acceleration will be

$$\ddot{x}(t) = \frac{q}{m_e} E(t), \tag{4}$$

where the notation $E(t) = |\vec{E}(t)|$ is used. The vector potential A, given by

$$-\frac{\partial A(t)}{\partial t} = E(t), \tag{5}$$

can be used to integrate equation (4), to get

$$x(t) = -\frac{q}{m_e}\left[A_0 \cdot (t - t_0) - \int_{t_0}^{t} \mathrm{d}t' A\left(t'\right)\right], \tag{6}$$

where $A_0 = A(t_0)$ is the vector potential at the ionisation time t_0. Assuming that the electric field is sinusoidal, the last term in the expression will cancel out as the electron leaves the beam. As the potential outside the beam is zero, the observed electron energy can be computed by differentiating equation (6) to get

$$\varepsilon = \lim_{t\to\infty} \frac{m_e \dot{x}^2}{2} = \frac{q^2}{2m_e} A_0^2. \tag{7}$$

Integrating equation (5), ε can be rewritten as

$$\varepsilon = \frac{q^2 E^2}{2m_e\omega^2} \sin^2(\omega t_0), \tag{8}$$

where ω is the field frequency and E the amplitude of $E(t)$. This gives the maximal observed energy $\frac{q^2E^2}{2m_e\omega^2} = 2U_\mathrm{p}$, where U_p, the ponderomotive energy, is the average potential energy of the electrons in the laser field. The value of U_p is explicitly calculated in section 2.4.

The exponentially decreasing pattern for $\varepsilon < 2U_\mathrm{p}$ can be seen in figure 2, where a typical ATI spectrum is shown. The peaks can be viewed as a result of the electron energy being proportional to the number of photons absorbed in the quantum mechanical interpretation.

As the direction of $\vec{E}$, due to linear polarisation, is constant, certain electron paths will lead back to the atom, illustrated in figure 3. Due to this, some freed electrons will scatter off the atom during the oscillation of the light wave. These electrons will scatter off the core at an angle θ, and gain a velocity $\dot{y}$ orthogonal to $\dot{x}$. Assuming completely

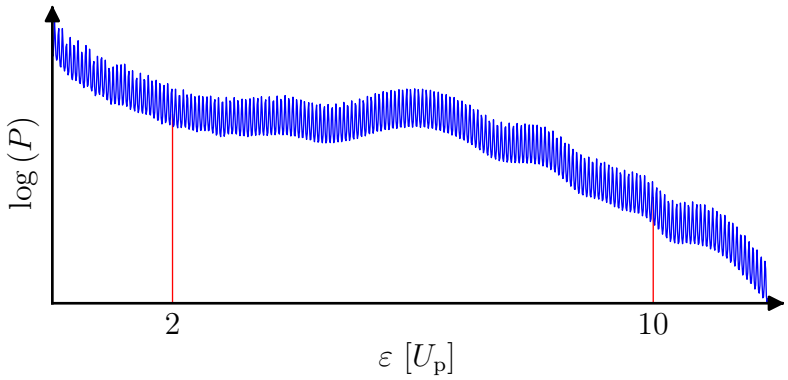

Figure 2: A typical ATI spectrum, showing the logarithm of the probability P of observing an electron with energy E during ATI. Below $2U_\mathrm{p}$, the directly ionised electrons are dominant. Between $2U_\mathrm{p}$ and $10U_\mathrm{p}$, a plateau is formed from rescattered electrons. Electrons observed with energies over $10U_\mathrm{p}$ are a result of quantum mechanical effects [3], such as smearing. The jagged nature of the spectrum is a result of the electrons absorbing energy in quanta – photons.

elastic rescattering, the electron velocity can be computed in the same manner as a newly ionised electron, but with an initial velocity. If $A_1 = A(t_1)$, The velocity of the rescattered electrons can be written

$$\begin{cases} \dot{x} = \frac{q}{m}\left[A_1 - A(t)\right] - \frac{q}{m}\left|A_1 - A_0\right|\cos(\theta) \\ \\ \dot{y} = \frac{q}{m}\left|A_1 - A_0\right|\sin(\theta) \end{cases}, \tag{9}$$

if $A_1 = A(t_1)$ is the vector potential at rescattering time t_1 [3]. As the potential will be zero outside the beam, the observed electron energy is

$$\varepsilon \propto \left\langle \dot{x}^2 + \dot{y}^2 \right\rangle. \tag{10}$$

The largest energy is given in the case of backscattering, giving an observed electron energy of

$$\varepsilon = \frac{q^2}{2m_e}\left(2A_1 - A_0\right)^2, \tag{11}$$

which can be maximised with respect to t_0 [and implicitly $t_1(t_0)$] to give $\varepsilon \approx 10U_\mathrm{p}$ [3]. The rescattered electrons therefore form a plateau in the region between $2U_\mathrm{p}$ and $10U_\mathrm{p}$, which can be seen in figure 2. The t_0 dependence of ε can be seen in figure 3.

The electric field of a short laser pulse can be described as the product of a Gaussian envelope, the amplitude of the pulse, and a carrier wave, responsible for its oscillation. For few-cycle laser pulses, the rapid change of amplitude translates into a broadening in the

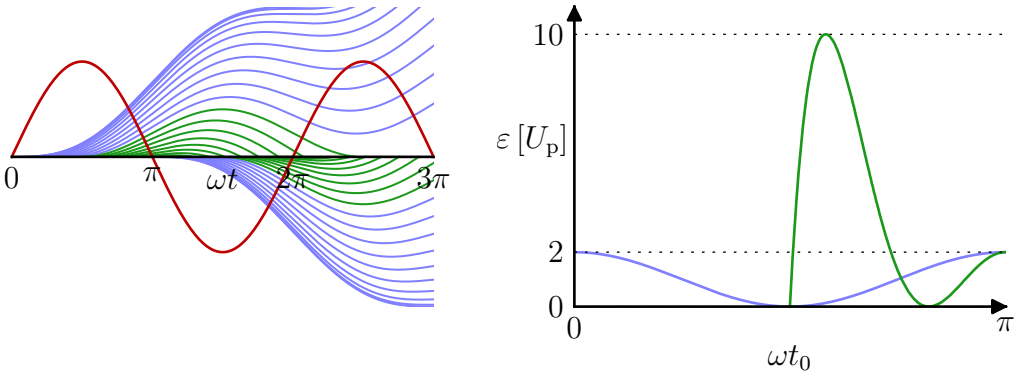

Figure 3: To the left the classical paths of the electrons excited through ATI during one period of the electric field are displayed. The force with which the electric field accelerates them is shown in red. The green paths bring the electrons back to the atom, opening the possibility of rescattering, whereas the blue paths lead to direct ionisation. The abscissa gives the phase of the electric field. On the ordinate, the amplitude of the electric field, and the distance from the atomic core to the electron paths is displayed in arbitrary units. To the right, the observed energy of the directly ionised electrons are given in blue, and the maximum energy of the rescattered electrons is given in green. the abscissa gives the excitation time, whereas the ordinate gives the observed electron energy.

frequency plane, and they can be viewed as a sum of several plane waves. This broadening will depend on the Carrier–Envelope Phase (CEP), and breaks the symmetrical character of the wave, as can be seen in figure 4. During ATI the distribution of electrons between the two directions of the electric field will be similarly affected, making it possible to gain information about the CEP by studying the electron distribution [4, 5]. This is also shown in figure 4.

For many-cycle laser pulses, the carrier wave can complete several cycles with approximately constant amplitude, making the broadening of the frequency less pronounced. However, the same effect can be obtained by using two different frequencies [6, 7]. The profile of the ATI spectrum depends on the phase difference ϕ, as illustrated in figure 5, between the respective carrier waves of the pulses.

As long as the intensities on one of the frequencies remains low, the electron paths, being approximated classically, will have the same appearance as those in figure 3. The same can be said for the electron energy, which depends only on the electron speed. The non-linear excitation rate, however can be greatly influenced by the constructive and destructive interference [8]. This is what changes the resulting ATI spectrum, as it changes the ionisation probability for electrons to be ionised at certain times, and as such with certain energies.

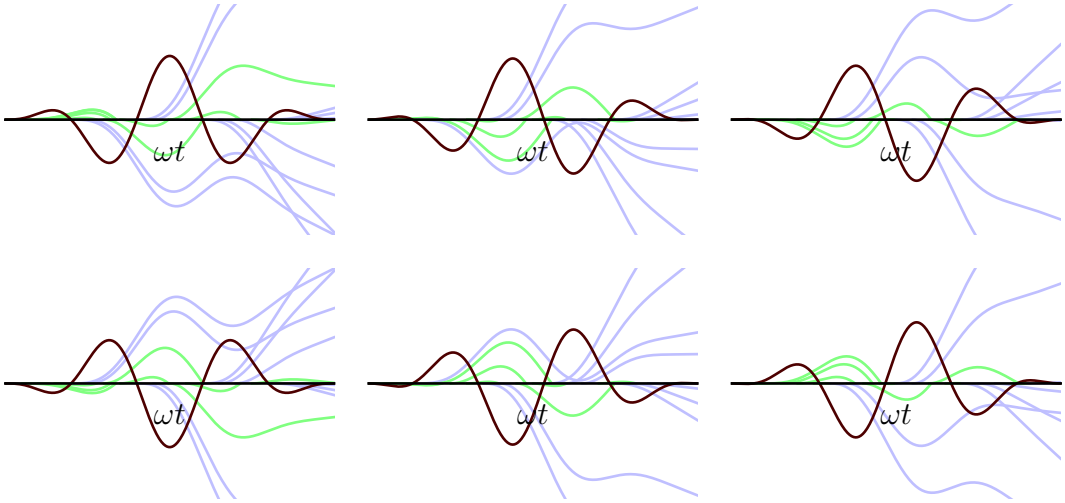

Figure 4: An illustration analagous to the first part of figure 3, but with a short pulse instead of a field with constant amplitude. The pulse has a $\cos^2$ envelope, and the value of its CEP goes from 0 to 2π, in steps of $\frac{1}{3}\pi$. Notice the asymmetry between the rows.

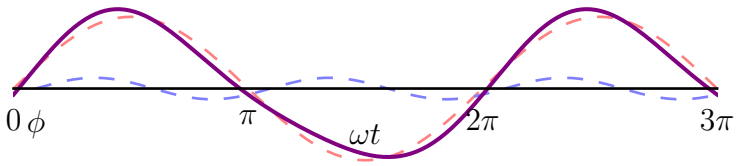

Figure 5: Illustration of the symmetry breakup of a high-intensity, low-frequency, field, due to a low-intensity, high-frequency field. Both fields displayed using dashed lines in the figure. The resultant field is shown as a solid line, and the phase difference ϕ is marked on the abscissa.

The influence of ϕ on the electron spectrum demonstrates its significance. It also enables the study of the observed electron spectrum to gain information about ϕ. This thesis aims to study the effect of ϕ during ATI, for the case when one of the carrier waves is a harmonic of the other, by studying the effect it has on the electron spectrum. The study is restricted to cases where the intensity of the high-frequency pulse is within a factor 0.001–0.15 of the low-frequency pulse intensity.

2 Method

2.1 ATI Calculations

This section summarises the code, more extensively discussed in [9], which generated the spectrum shown in figure 2, and which was used for the ATI calculations for this thesis. It solves the Time-Dependent Schrödinger Equation (TDSE) for single-active electron approximation potentials on the form

$$V(\vec{r}) = \sum_{\ell} V_{\ell}(r) |\ell\rangle \langle\ell| - \frac{1}{r}, \tag{12}$$

where $\vec{r}$ is the position vector with its origin in the atomic core and ℓ the angular momentum. The grid is discretised along $r = |\vec{r}|$, and is described by a truncated base $|\ell\rangle$ in the angular plane.

The z axis is chosen to be parallel with the electric field. For the electron wavefunction $|\psi\rangle$ this gives the TDSE in the length gauge,

$$\mathrm{i}\frac{\partial}{\partial t} |\psi_l\rangle = [H_0 + E(t)\, z] |\psi_l\rangle, \tag{13}$$

where H_0 is the Hamiltonian with electric field strength zero. One disadvantage of this form is that as z increases, the $E(t)\, z$ term can cause great numerical inaccuracy. To avoid this, the TDSE is written using the velocity gauge,

$$\mathrm{i}\frac{\partial}{\partial t} |\psi_v\rangle = \left[H_0 - iA(t)\frac{\partial}{\partial z}\right] |\psi_v\rangle, \tag{14}$$

where $\hat{A}$ is the vector potential, given by equation 5.

This is convenient for large z, but for small z, the same problem seen in the length gauge for large z, can be observed. For this reason, the length-gauge is used for small z, and the velocity gauge for large z. An intermediate region is also defined, where the TDSE is integrated separately in both gauges. As the areas over which the two gauges are computed ends at the respective edges of this region, their boundary conditions will give a contribution to the calculations. In order to counter this, the two gauges are matched, as illustrated in figure 6.

The energy of the electrons is given to them by the photons they absorb, as are their ℓ. Thus, the total number of partial waves required, ℓ_{tot}, will be determined by the ℓ values of the high energy electrons. Because both the range from the core and the kinetic energy depends on the velocity, ℓ_{tot} will be determined in the velocity gauge.

The transformation between the gauges is

$$|\psi_l\rangle = e^{-\mathrm{i}[A(t)z + \Phi(t)]} |\psi_v\rangle, \tag{15}$$

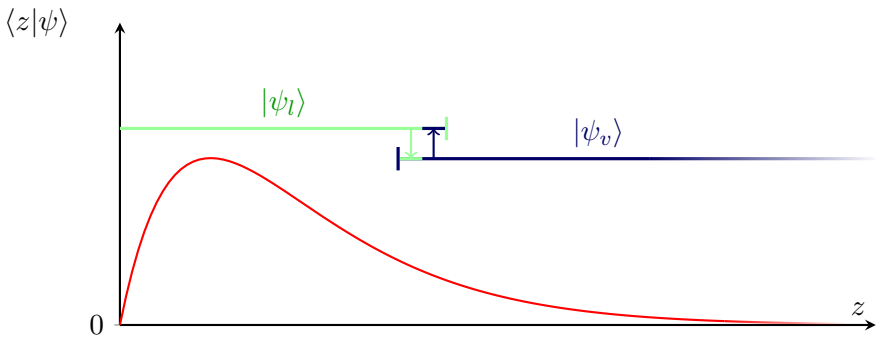

Figure 6: An illustration of the regions the two respective gauges are used to compute the wavefunction. Far from the atom, the velocity gauge is used, whereas the length gauge is used near the core. The gauges overlap in a small region. To avoid effects from the boundary conditions at the edges of this region, the two solutions are matched, as illustrated with arrows in the figure.

where

$$\frac{\partial \Phi\left(t\right)}{\partial t} = \frac{1}{2} A^2\left(t\right), \tag{16}$$

largely removing the ket phase factor in the velocity gauge, and thereby reducing ℓ_{tot}.

2.1.1 Convergence in ℓ

Photons have angular momentum ± 1, and the code uses a finite basis in the ℓ direction. As the energy of the electrons are proportional to the number of photons absorbed, the energy up to which the electron spectrum accurately can be modelled is proportional to the the number of basis functions used in ℓ.

The number of ℓ values needed equals the total energy section studied, multiplied by the number of photons per unit of energy. Thus, optimally,

$$\ell_{\text{tot}} \approx 10 U_{\text{p}} \cdot \frac{1}{\hbar\omega}. \tag{17}$$

Since the simulation time is proportional to the number of grid points, it was not feasible to fulfil the convergence criterion of equation (17). This despite the use of mixed gauges to decrease ℓ_{tot}. Instead, ℓ_{tot} was increased incrementally, as the convergence of the electron spectrum was calculated. The code only accepted odd values of ℓ_{tot}, so a stepsize of two was used. As a requirement for convergence for the vectors P_i^ℓ describing the electron spectrum, with momentum indicated by superscript and vector index indicated by subscript,

containing the computed electron spectra up to $10U_\mathrm{p}$,

$$\begin{cases} \frac{1}{N}\sqrt{\sum_i \left(\frac{P_i^\ell - P_i^{\ell+1}}{P_i^\ell + P_i^{\ell+1}}\right)^2} & < 10^{-4} \\ \max_i \left|\frac{P_i^\ell - P_i^{\ell+1}}{P_i^\ell + P_i^{\ell+1}}\right| & < 10^{-2} \end{cases} \tag{18}$$

was used.

2.1.2 Pulse Envelope Shape

Envelopes of short laser pulses are often approximated as having a Gaussian shape. A drawback of using Gaussian pulses for numerical computations is that they have no finite cutoff point. The electric field and the vector potential must be approximately continuous in order to model a physical system. Thus, in order to keep a high numerical accuracy, a high number of time steps is required. A Gaussian is displayed in figure 7(a).

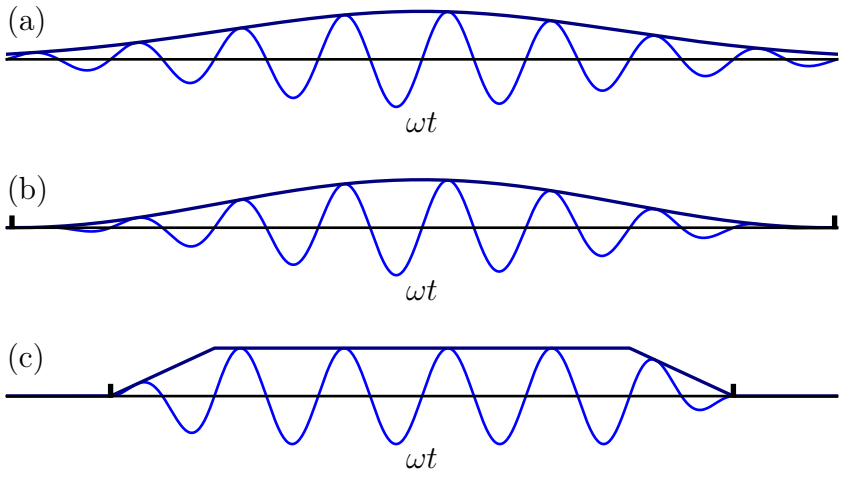

Figure 7: Different envelope shapes considered in this thesis. In (a), a Gaussian is displayed, in (b), a $\cos^2$ shape, and in (c) a trapezoidal.

A Gaussian has roughly the same shape as a $\cos^2$ function, as can be seen when comparing figures 7(a) and 7(b). By using a $\cos^2$ envelope, the general shape of a Gaussian can be obtained, with the additional benefit of cutoff points.

A third pulse envelope shape is that of a trapezoid. For trapezoidal envelopes, the only frequency broadening comes from the linear slopes at the beginning and end of the

pulse. The pulse can therefore be made long enough to have the majority of asymmetry contribution come from the interaction the two carrier waves of different frequency, during the plateau of constant amplitude, which makes up the bulk of the envelope. It is also easy to keep a constant intensity by using trapezoidal pulses. Unless otherwise stated, pulse envelopes used in this paper were trapezoidal, the slopes near the edges of the envelopes used here were one period of the low-frequency pulse each, whereas the plateau was six periods long.

As Gaussian pulses are infinite, the entire pulse can not be modulated, as it would require infinitely many time steps. Instead, the calculations were done over time T, with a constant number of gridpoints per unit of time, and the center of the gaussian pulse at time $\frac{T}{2}$. The convergence criterion

$$\begin{cases} \frac{1}{N}\sqrt{\sum_i \left(\frac{P_i^T - P_i^{T+\frac{4\pi}{\omega}}}{P_i^T + P_i^{T+\frac{4\pi}{\omega}}}\right)^2} & < 10^{-4} \\ \max_i \left|\frac{P_i^T - P_i^{T+\frac{4\pi}{\omega}}}{P_i^T + P_i^{T+\frac{4\pi}{\omega}}}\right| & < 10^{-2} \end{cases}, \tag{19}$$

where the superscript indicates the total time simulated, was, analogously to equation (18), used.

2.1.3 Method of Sweeping

In order to generate images according to section 2.2.2 below, data must be gathered for several different ϕ. Here, three methods for numerically sweeping over values of ϕ, displayed in figure 8, are considered.

The first method, displayed in figure 8(a), entails sweeping over different values of the low-frequency CEP. This has the disadvantage of significantly altering the pulse shape, which may cause secondary effects, and thus risk obscuring the effect from interactions with the high-frequency field.

The second method, shown in figure 8(b), is analogous to the first, but the sweep is done over the high-frequency, rather than the low-frequency, CEP. This causes the same secondary effects as the first method, but to a lesser degree, due to the relative pulse intensity of the waves. The effects from the interaction will, however, retain its magnitude. Thus, this method is preferable to the former. It was used to generate all data and figures in this study, unless otherwise explicitly stated.

The third and final method considered, illustrated in figure 8(c), was to keep the respective pulse shapes constant, and to instead add a time offset to the smaller pulse. By changing the time offset, ϕ can be changed while avoiding the effects associated with either of the pulse-shapes changing. When using trapezoidal envelopes, as in figure 8, the high-frequency pulse, if being kept within the amplitude plateau of the low-frequency pulse, can

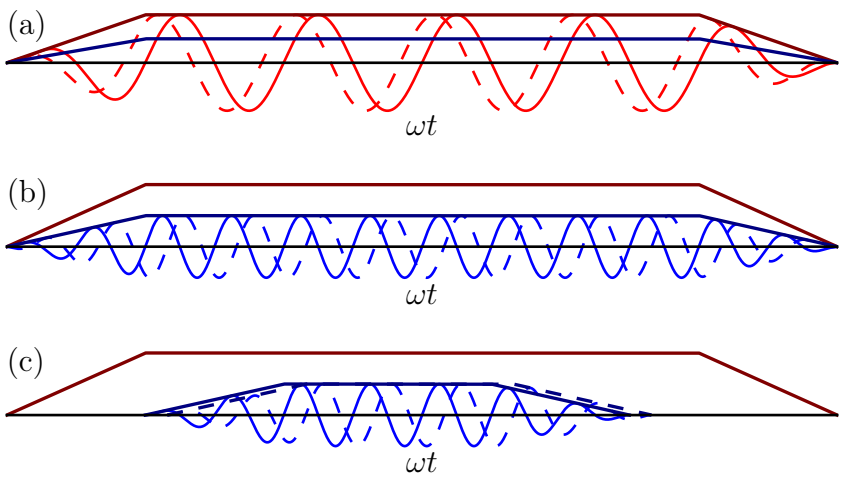

Figure 8: Illustration of different methods for sweeping over ϕ. In (a), the CEP of the low-frequency wave is changed, in (b), that of the high-frequency wave, and in (c) the high-frequency wave is given an offset. The effect of the phase change between the solid and the dashed wave on the relative peak phase between the low- and high-intensity pulses is the same in all three subfigures.

be viewed as a relatively weak laser pulse in a constant laser field. One drawback of this method is that the relevant pattern will only be present during part of the total simulation time. Thus, either the computational time has to be increased, or the effect on the ATI spectrum will be less pronounced.

When sweeping over different ϕ, it should be noted that changing the phase of the low-intensity wave of frequency $k\omega$ has k times the effect on the peak location as changing the phase of the high-frequency wave by an equal amount. This can be seen in figure 8, where the absolute of the phase change between the solid and the dashed wave in (a) is half of that in (b), but the absolute of the change in peak location is the same.

2.2 Even Harmonics

2.2.1 Selection of the High and Low Energy Ranges

Consider an ATI spectrum, generated by a pulse where the low-intensity wave is the second harmonic of the high-intensity wave. As can be seen in figure 5, the contribution of the high-frequency field is asymmetrical between the positive and negative field direction: if there is constructive interference prior to the low-intensity peak in the positive direction of the field, there is destructive interference prior to the low-intensity peak in the negative direction of the field.

By considering the electrons being excited in the two directions of the field separately,

the asymmetry can be studied further. In the positive direction of the field there will be one energy region (one region of ionisation times) with constructive interference, and one with destructive. In the negative direction the same regions will be inverted. This gives one set of times contributing to an overrepresentation of electrons in the positive field direction, and one contributing to an overrepresentation in the negative field direction.

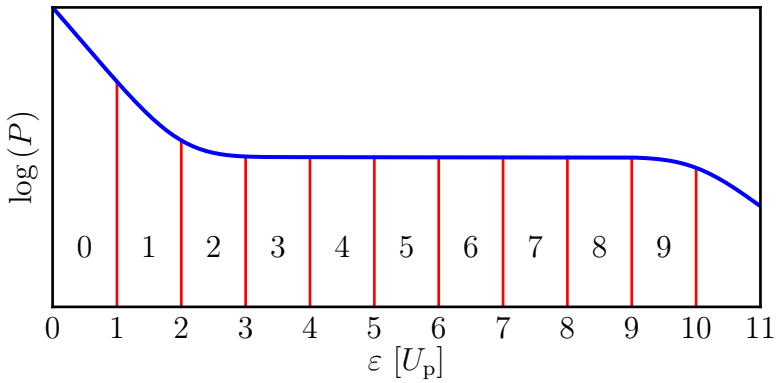

Figure 9: In blue, a simplified version of the general characteristics of an ATI spectrum is given. The red lines illustrates how the electron spectrum was divided into ten equidistant sections, enumerated from 0 to 9. The abscissa gives the Energy in units of U_p, whereas the ordinate gives the logarithm of the probability density of electrons.

The probability of observing a free electron as a function of energy is highly dependent on ϕ shape [7]. When observing either an increase or a decrease in the low energy spectrum, the reverse should appear in the high energy spectrum. In order to gain a measure of the asymmetry, one low, and one high, energy region, denoted ε_l and ε_h respectively, were compared.

To make the selection of ε_l and ε_h, the spectrum up to $10U_\mathrm{p}$ was divided into 10 equally spaced sections, enumerated 0 to 9, as illustrated in figure 9. Each energy region was then generated from one, or several neighbouring, sections. The regions were chosen to be non-overlapping. For quick reference, a four digit label was associated with each possible selection of areas. The first pair of digits in the label describes the low and the second pair the high region. For each pair of digits, the first denotes the number of sections included in the region, and the second digit the index of the first included section. This is exemplified in Table 1.

To find the most useful ε_l and ε_h, every possible division in accordance with the aforementioned method were tested. In total 495 divisions were produced, out of which the ones with the most beneficial properties could be selected. A similar division into n areas would lead to $N(n)$ divisions, where

Table 1: Examples of the division of the ATI spectrum into ε_l and ε_h. The table gives the label of each division, along with the sections included in, and the energy range covered by, the ε_l and ε_h.

Label	Sections		Energy Range (U_p)	
	ε_l	ε_h	ε_l	ε_h
4136	$1, 2, 3, 4$	$6, 7, 8$	1–5	6–9
2113	$1, 2$	3	1–3	3–4
1041	0	$1, 2, 3, 4$	0–1	1–5
2219	$2, 3$	9	2–4	9–10

$$N(n) = \frac{1}{24}\left(n^4 + 2n^3 - n^2 - 2n\right). \tag{20}$$

For each division, measures of ϕ of varying quality were created according to section 2.2.2 below.

2.2.2 Representation in the $A_\mathrm{l} - A_\mathrm{h}$ and $\theta - \phi$ planes

Call the probability of observing an electron per unit of energy as a function of energy $P_+(\varepsilon)$ and $P_-(\varepsilon)$, where the subscripts indicate in which direction of the electric field they were observed. As in [4, 5], measures of the respective asymmetries of ε_l and ε_h, A_l and A_h, were defined as

$$\begin{cases} A_\mathrm{l} = \dfrac{\displaystyle\int_{\varepsilon_\mathrm{l}} P_+(\varepsilon) - P_-(\varepsilon)\,\mathrm{d}\varepsilon}{\displaystyle\int_{\varepsilon_\mathrm{l}} P_+(\varepsilon) + P_-(\varepsilon)\,\mathrm{d}\varepsilon} \\ \\ A_\mathrm{h} = \dfrac{\displaystyle\int_{\varepsilon_\mathrm{h}} P_+(\varepsilon) - P_-(\varepsilon)\,\mathrm{d}\varepsilon}{\displaystyle\int_{\varepsilon_\mathrm{h}} P_+(\varepsilon) + P_-(\varepsilon)\,\mathrm{d}\varepsilon} \end{cases}. \tag{21}$$

If the electric field amplitude of a pulse can be approximated as constant, a change in ϕ of π radians corresponds to a sign change of the asymmetry and a time displacement, as illustrated in figure 10. For many-cycle pulses the majority of contributions to the symmetry breakup can be seen as taking place over long periods with approximately constant amplitude. Thus, the time displacement can be ignored. This relationship can be written as

$$\phi \to \phi + \pi \Rightarrow \begin{cases} A_\mathrm{l} \to -A_\mathrm{l} \\ A_\mathrm{h} \to -A_\mathrm{h} \end{cases}, \tag{22}$$

and is illustrated in the extrapolation of figure 11(a) to 11(b).

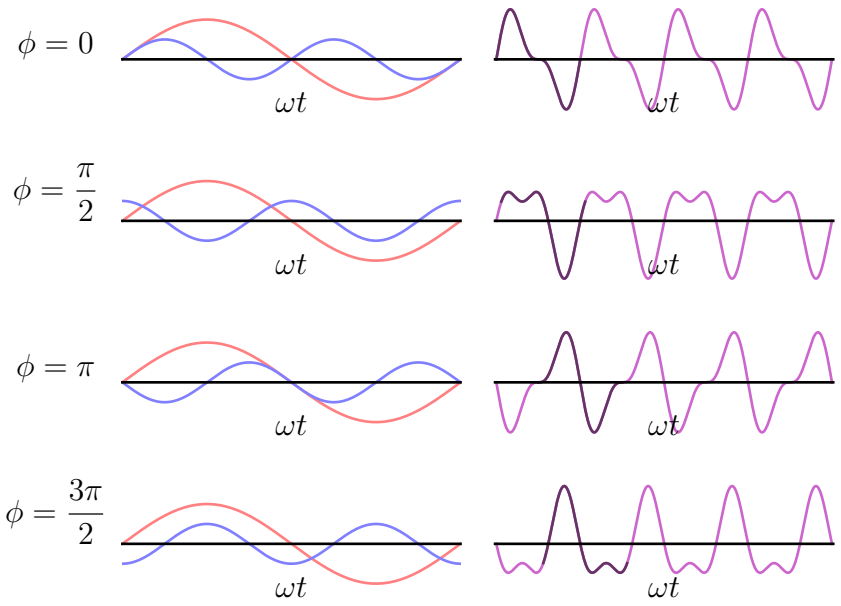

Figure 10: To the left the first and the second harmonic of a frequency ω is displayed over one period, to the right their sum is shown over several. Between each row ϕ is changed by $\frac{\pi}{2}$. Comparing the first and third or the second and fourth row illustrates how changing ϕ by π radians corresponds to a sign change of the total asymmetry of the electric field.

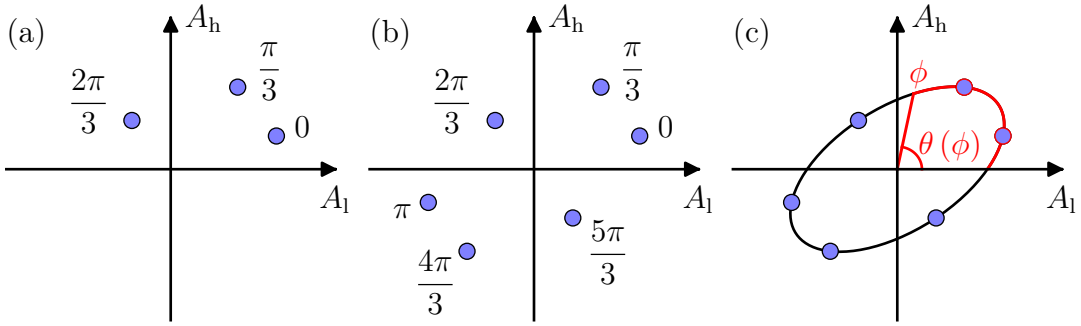

Figure 11: An illustration of the $A_\mathrm{l} - A_\mathrm{h}$ plane. In (a) the positions of a two-colour pulse in the $A_\mathrm{l} - A_\mathrm{h}$ plane have been given for $\phi \in \{0, \frac{\pi}{2}, \frac{2\pi}{3}\}$. An extrapolation of the values in (a) based on equation 22 can be seen in (b). In (c) the ϕ dependent angle θ is shown.

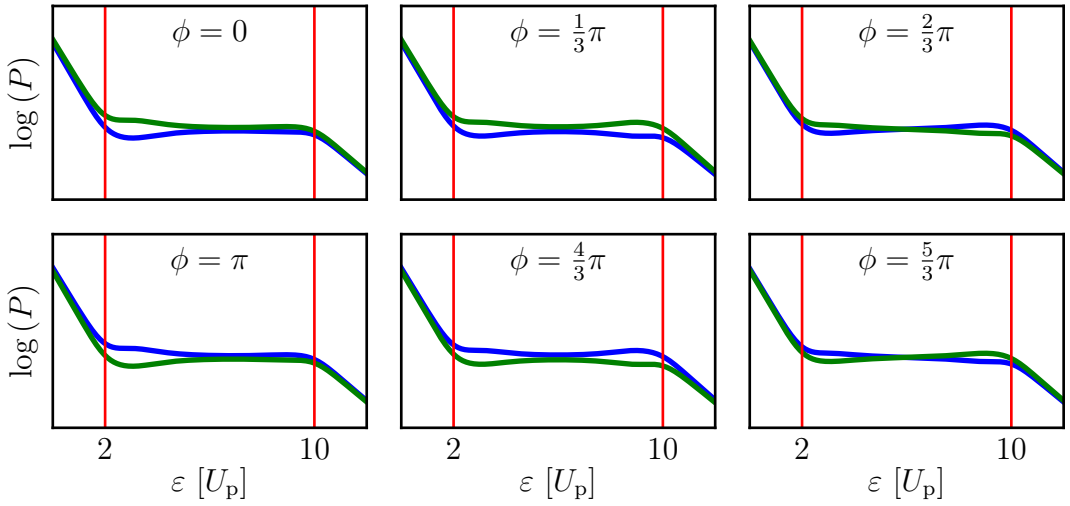

Figure 12: An illustration of the general characteristics of potential ATI spectra corresponding to the coordinates marked in figure 11. Here, P_+ is given in green and P_- in blue. The first row shows the ATI spectra for the coordinates marked in figure 11(a), and second row shows the ATI spectra corresponding to the coordinates added in figure 11(b).

In figure 12, ATI spectra with the same general characteristics represented as those represented by the coordinates in figure 11 is shown. For $\phi = 0$, P_+ is greater than P_- for both high and low ε, but especially for low, giving a large, positive, A_l and a small, positive A_h. For $\phi = \frac{\pi}{3}$, P_+ is significantly larger than P_- for both the low and high energy spectra, resulting in both A_l and A_h being large and positive. At $\phi = \frac{2\pi}{3}$, P_- has become larger than P_+ for high, and only for high, ε, resulting in a negative A_l, but a positive A_h. Because the difference between P_+ and P_- is small for both high and low ε, A_l and A_h will also be small.

The angular coordinate in the A_l – A_h plane is here called θ, and is displayed in figure 11. For certain shapes in the A_l – A_h plane, such as ovals, it can be uniquely matched to ϕ. This is illustrated in figure 13, for the case of figure 11(c). The energy regions, generated according to section 2.2.1, providing the most useful shapes were selected, and the matching of θ and ϕ was used as a measure of ϕ.

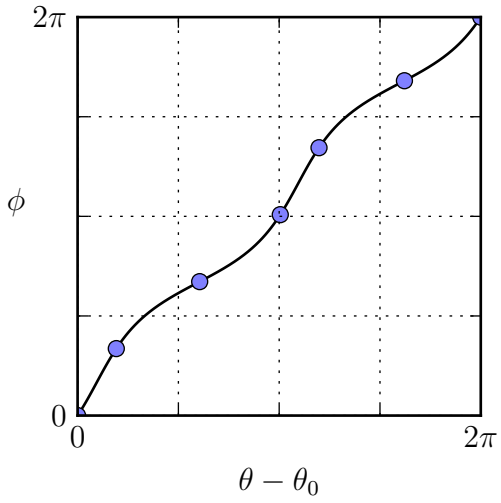

Figure 13: An illustration of how ϕ can be deduced from θ, using the values in figure 11. For convenience $\theta_0 = \theta|_{\phi=0}$ has been subtracted from θ.

The same line of reasoning which was used to derive equation (22) also gives

$$\phi \to \phi + \pi \Rightarrow \begin{cases} P_+ \to P_- \\ P_- \to P_+ \end{cases}, \tag{23}$$

and therefore

$$\begin{cases} A_\mathrm{l}\left[P_+\left(\phi\right), P_-\left(\phi\right)\right] \approx A_\mathrm{l}\left[P_+\left(\phi\right), P_+\left(\phi+\pi\right)\right] \\ \\ A_\mathrm{h}\left[P_+\left(\phi\right), P_-\left(\phi\right)\right] \approx A_\mathrm{h}\left[P_+\left(\phi\right), P_+\left(\phi+\pi\right)\right] \end{cases}. \tag{24}$$

In other words, it is possible to get a measure of the asymmetry while observing only the electrons travelling in one of the ionisation directions.

2.2.3 Inverse transformations

For A_l, equation (21) can be rewritten as

$$A_\mathrm{l} = \frac{\Gamma^+ - \Gamma^-}{\Gamma^+ + \Gamma^-}, \ A_\mathrm{l} \in [-1, 1] \tag{25}$$

, where

$$\Gamma^\pm = \int_{\varepsilon_\mathrm{l}} \mathrm{d}\varepsilon P_\pm\left(\varepsilon\right). \tag{26}$$

This can in turn be written as

$$\Gamma^{+} = \frac{1 + A_{\mathrm{l}}}{1 - A_{\mathrm{l}}} \cdot \Gamma^{-}, \tag{27}$$

and the same principle can be applied for ε_{h}. From equation (25) it can be seen that A_{l} goes from -1 to 1 – the cases where all electrons with energy ε_{l} are observed leaving the laser in the same direction. To put the area $A_{\mathrm{l}} \in (-1, 1)$ into perspective, the cases where A_{l} takes the values of 0.2, 0.5, and 0.8 corresponds to overrepresentations of P^{+} over P^{-} at ε_{l} by factors 1.5, 3, and 9 respectively.

2.3 Odd Harmonics

For the case when the low-intensity pulse has a frequency on the form $(2k + 1)\,\omega, k \in \mathbb{N}$, the total electric field will not be asymmetrical, since

$$E(\omega t) \propto \sin(\omega t) + \sin((2k + 1)\,\omega t + \phi), \tag{28}$$

fulfils

$$E(\omega t) = -E(\omega t + \pi), \tag{29}$$

as illustrated in figure 14. This means that the ATI spectrum will be affected symmetrically along the directions of the electric field, and that, instead of the asymmetry, the total effect the constructive and destructive interference has on the ionisation probability can be measured.

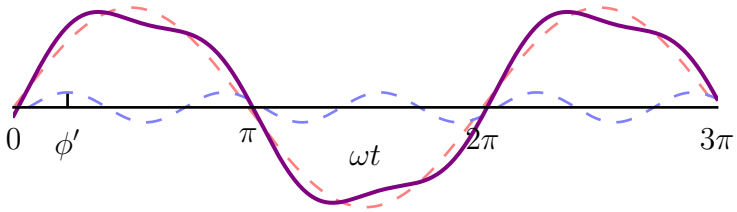

Figure 14: Illustration of the field resulting from the sum of two sinusoidal carrier waves, one low-intensity field with frequency ω and a high-intensity field with frequency 3ω. The carrier waves are displayed using dashed lines, and their sum using a solid line. The phase of one of the low-intensity maxima, ϕ', is marked on the abscissa.

In order to measure how the ionisation probability of different energies changes depending on ϕ', the quantity

$$\Delta P\left(\phi', \varepsilon\right) \equiv \frac{P\left(\phi', \varepsilon\right) - \widetilde{P}\left(\varepsilon\right)}{\widetilde{P}\left(\varepsilon\right)} \tag{30}$$

was defined, where the ϕ'-average,

$$\widetilde{P}\left(\varepsilon\right) = \frac{1}{N}\sum_{i=0}^{N-1} P\left(\phi_i', \varepsilon\right), \tag{31}$$

was used to normalise the function, and P was computed for the linearly spaced $\phi' \in \left(\phi_0', \phi_1', \ldots, \phi_{N-1}'\right)$. When considering the asymmetry discussed in section 2.2, the spectrum was analysed by integrating over ε, which countered noise. For odd harmonics, however, where the excitation probability of individual energies is considered, only the peak energies are taken into account.

2.4 The Ponderomotive Energy of Two-Colour Fields

The maximal energy electrons can gain during the rescattering process is approximately $10U_\mathrm{p}$. For this reason, the spectrum is only studied for energies up to $10U_\mathrm{p}$. Consider a two-colour electric field $\vec{E}$, on the form

$$\vec{E} = \vec{E}_\omega \sin\left(\omega t\right) + \vec{E}_{k\omega} \sin\left(k\omega t + \phi\right), \ k \in \mathbb{N} \tag{32}$$

where the two electric field envelopes $\vec{E}_\omega$ and $\vec{E}_{k\omega}$ are parallel. The force F on a free electron in the direction of the electric field is

$$F = q \cdot E_\omega \left[\sin\left(\omega t\right) + E_\mathrm{rel} \sin\left(k\omega t + \phi\right)\right], \tag{33}$$

where E_rel is the relative magnitude of the electric fields. Integrating twice gives the electron distance x from the core, for different ionisation conditions, as a function of time. However, for the purpose of computing U_p, the cycle-averaged energy that can be gained from the field, the position and velocity at ionisation are irrelevant. Thus, for an electron with mass m_e, the integration constants are chosen so that

$$x = -\frac{qE_\omega}{m_e\omega^2}\left[\sin\left(\omega t\right) + \frac{E_\mathrm{rel}}{k^2}\sin\left(k\omega t + \phi\right)\right]. \tag{34}$$

In order to compute U_p using

$$U_\mathrm{p} = \frac{1}{2} m_e \omega^2 \left\langle x^2 \right\rangle_t, \tag{35}$$

it can be noted that $\langle x^2 \rangle_t$ can be divided into three separate terms,

$$\langle x^2 \rangle_t \propto \langle \sin^2(\omega t) \rangle_t + \frac{2E_{\text{rel}}}{k^2} \langle \sin(\omega t) \sin(k\omega t + \phi) \rangle_t + \frac{E_{\text{rel}}^2}{k^4} \langle \sin^2(k\omega t + \phi) \rangle_t . \tag{36}$$

The first and third terms become

$$\langle \sin^2(\omega t) \rangle_t = \langle \sin^2(k\omega t + \phi) \rangle_t = \frac{1}{2}, \tag{37}$$

whereas the second term is zero, as $\sin(\omega t)$ and $\sin(k\omega t + \phi)$ are orthogonal over the period $\frac{2\pi}{\omega}$. Using the relative intensity $I_{\text{rel}} = E_{\text{rel}}^2$, U_{p} can be written as

$$U_{\text{p}} = \frac{q^2 E_\omega^2}{4 m_e \omega^2} \left(1 + \frac{I_{\text{rel}}}{k^4} \right). \tag{38}$$

The maximal relative intensity considered in this project is $I_{\text{rel}} = 0.15$, and the minimum $k = 2$. This gives a maximum increase in U_{p} of less than a factor 1.01 compared to the monochromatic case of $I_{\text{rel}} = 0$. Given that information about A_{l} and A_{h} is gathered by integrating the electron spectrum over units of whole U_{p}, a change of factor 1.01 in U_{p} will not have a significant effect, and need not be considered when selecting ε_{l} and ε_{h}. For k larger than 2 the change to U_{p} will become even smaller, and $k = 1$ can simply be interpreted as a change in the total amplitude of a monochromatic wave, by a factor $1 + I_{\text{rel}}$.

3 Results and Discussion

3.1 Asymmetry as a Function of ϕ

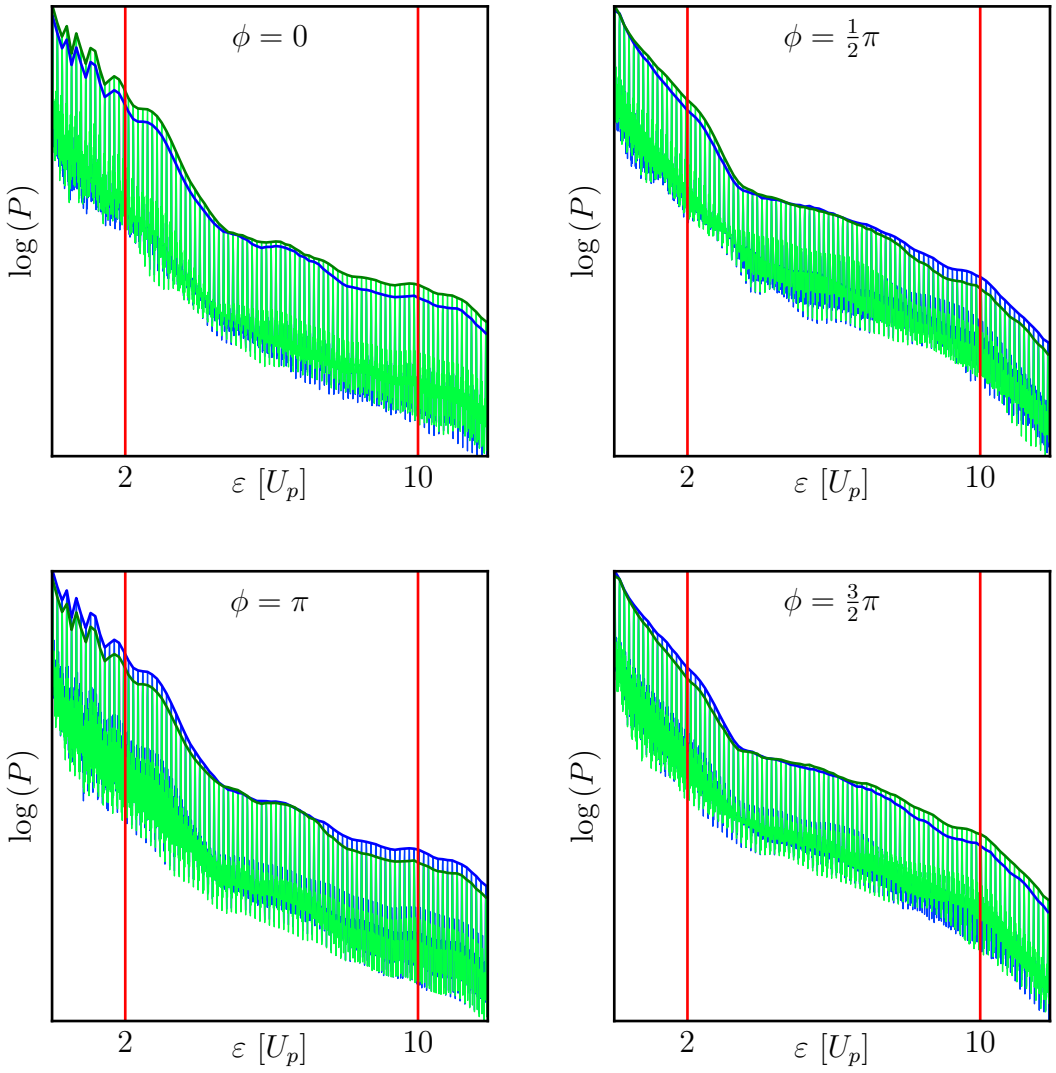

Figure 15: The spectra along the two directions of the z axis of a two colour pulse with $I_{\text{rel}} = 0.15$. Electrons observed in the two directions are marked in blue and green, respectively. In the four figures, ϕ takes the values of 0, $\frac{\pi}{2}$, π and $\frac{3\pi}{2}$.

As can be seen in figure 15, the ATI spectrum changes drastically with ϕ. In the first figure, every peak of the green spectrum is high enough to obscure its corresponding blue peak. In the second figure, the blue peaks are greater than the green ones in the high-energy part of the spectrum, and by the third figure this pattern is representative for almost the entire spectrum. By the fourth figure, the green energy spectrum once again starts to dominate in the high-energy region, and so the pattern starts over.

The asymmetry of an ATI spectrum as a function of ϕ can be represented in the $A_\mathrm{l} - A_\mathrm{h}$ plane, as explained in section 2.2.2. Two such representations, created using the same data as was used in figure 15, can be found in figure 16. In ATI spectra, such as those in figure 15,

$$P_+(\varepsilon, \phi) - P_-(\varepsilon, \phi) \approx P_-(\varepsilon, \phi + \pi) - P_+(\varepsilon, \phi + \pi), \tag{39}$$

which translates into the approximately symmetrical $A_\mathrm{l} - A_\mathrm{h}$ representations that can be seen in figure 16.

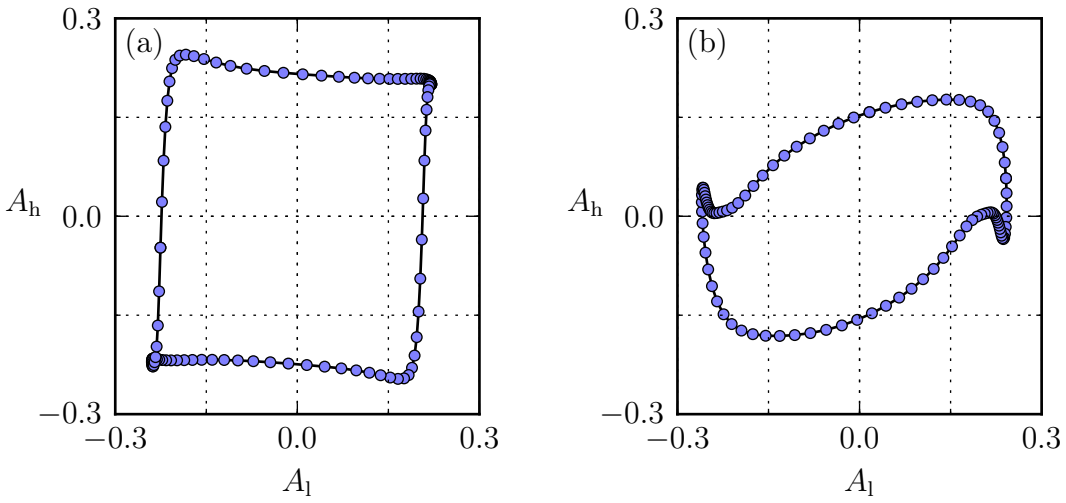

Figure 16: The $A_\mathrm{l} - A_\mathrm{h}$ representation for two divisions of the spectra seen in figure 15. In (a) the 4219 division and in (b) the 1125 division is given. It can be seen how equation (22) translates into an approximate symmetry in the $A_\mathrm{l} - A_\mathrm{h}$ plane.

3.2 Phase–Angle Matching

As can be seen in figure 17(a), it is possible to get an almost ellipsoidal $A_\mathrm{l} - A_\mathrm{h}$ representation of the electron spectrum. In figure 17(b), the corresponding, and almost linear, relation between θ and ϕ is displayed.

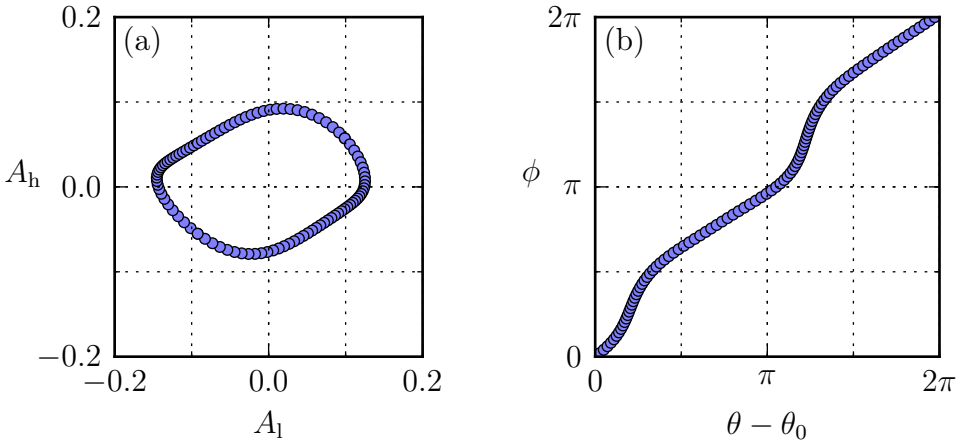

Figure 17: In (a) the $A_\mathrm{l} - A_\mathrm{h}$ representation, and in (b) the $\theta - \phi$ matching, of the 4055 division of two pulses with $I_\mathrm{rel} = 0.01$, is given.

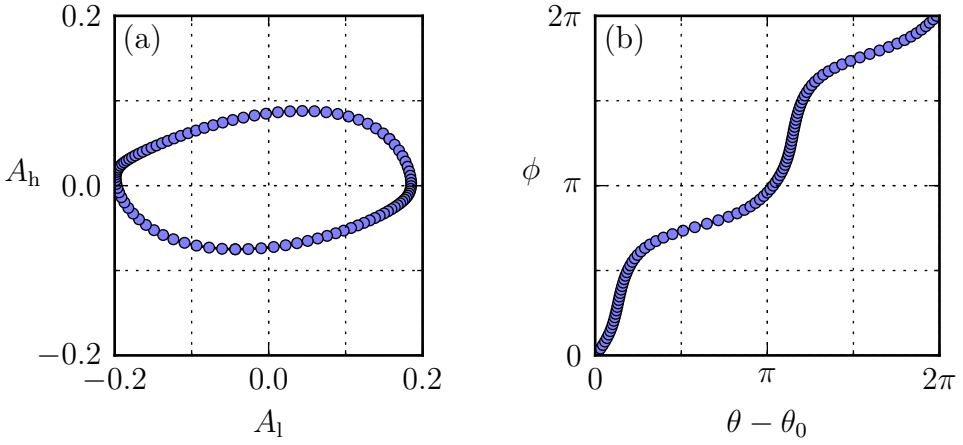

Figure 18: The 1145 division of the data used in figure 17.

Although the division 4055 was chosen for figure 17 due to its almost linear $\theta - \phi$ representation, linearity is not necessarily optimal. Consider instead figure 18(b). Despite the uncertainty in determining ϕ being high if $\phi \approx \frac{\pi}{3}$, the 1145 division will be ideal to get the exact value of ϕ if $\phi \approx \frac{3\pi}{4}$ – the flat slope near $\theta - \theta_0 = \frac{2\pi}{3}$ minimises the effect of any errors in θ or θ_0. It is therefore possible to improve the accuracy of ϕ by choosing a good division of the energy spectrum, something which can be done without the need to gather

new measurement data.

Despite the advantages, there are risks associated with choosing the smallest $\frac{\partial\phi}{\partial\theta}$. A flat slope in the $\theta-\phi$ plane, such as that in figure 19(b), tends to correlate with, and sometimes is the result of, values near the origin point in the $A_\mathrm{l} - A_\mathrm{h}$ plane, as exemplified in figure 19(a). Because of this a small absolute change in the $A_\mathrm{l} - A_\mathrm{h}$ plane might translate into a large change in ϕ.

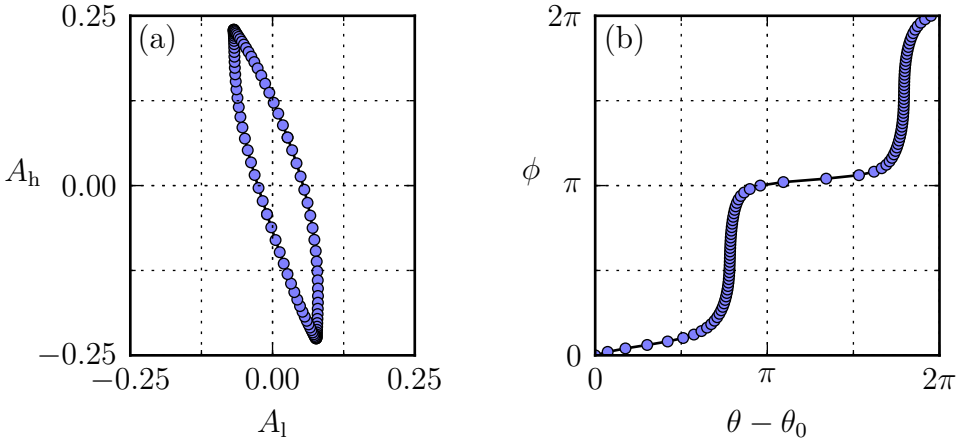

Figure 19: The 1163 division of the data is even more extreme than the 1327 division.

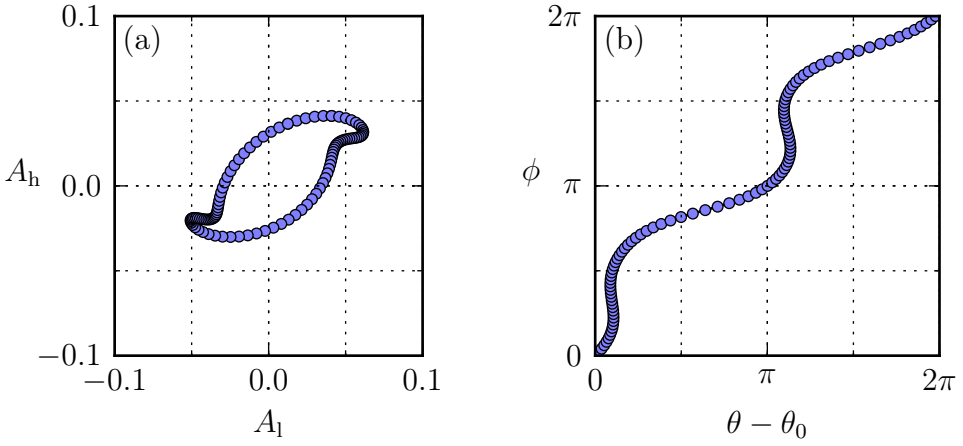

Figure 20: For some divisions and ATI spectra, here the 1415 division of the same data as in previous figures, $\theta\,(\phi)$ is not injective.

The function $\theta(\phi)$ is not always injective, as can be seen in figure 20(b). The shapes near $(A_\mathrm{l}, A_\mathrm{h}) = \pm(0.05, 0.05)$ in figure 20(a) give an ambiguous reading of ϕ from θ, and such divisions of the energy spectrum should be avoided.

3.3 Single Detection Direction

By using equation (24), it is possible to generate the $A_\mathrm{l} - A_\mathrm{h}$ and $\theta - \phi$ representations of a ATI spectrum while observing only those electrons travelling in one direction of the electric field. This is illustrated by figure 21.

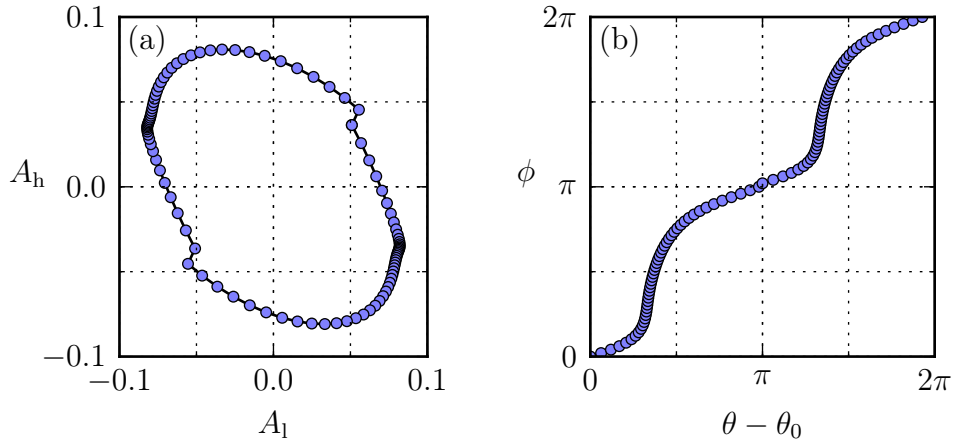

Figure 21: The 2225 division of a two-colour pulse with $I_\mathrm{rel} = 0.01$. Instead of observing the electrons travelling in both directions, equation 24 was used.

As can be seen in figure 21(a), the circle border is discontinuous on two points on the $A_\mathrm{l} - A_\mathrm{h}$ plane. This happens when $\phi = \pi - \delta \to \phi = \pi + \delta$. The reason for this is that, if N different ϕ values, $\phi \in (\phi_0, \phi_1, \ldots, \phi_N)$, have been used to generate the circle, A_l will change as

$$A_\mathrm{l} = A_\mathrm{l}\left[P_+\left(\phi_{N/2}\right), P_+\left(\phi_N\right)\right] \longrightarrow A_\mathrm{l} = A_\mathrm{l}\left[P_+\left(\phi_{N/2}\right), P_+\left(\phi_0\right)\right], \tag{40}$$

in order to accommodate the fact that no values ϕ_i have been computed for $i > N$. The same argument can be made for A_h. The discontinuity does not appear as clearly in the $\theta - \phi$ plane as in the $A_\mathrm{l} - A_\mathrm{h}$ plane, however it will appear at $\theta - \theta_0 = \phi \in \{0, \pi, 2\pi\}$, and can be seen in figure 21(b).

Due to the use of the same measurement data for A_l and A_h being used at $\phi = \phi_i$ as $\phi = \phi_i + \pi$, the $A_\mathrm{l} - A_\mathrm{h}$ representation of the ϕ sweep will be precisely symmetrical. This is illustrated in figure 21(a), and figure 21(b), where $\phi(\theta - \theta_0) = \phi(\theta - \theta_0 + \pi)$, for $\theta - \theta_0 < \pi$.

3.4 Method of Sweeping

In figure 22 the result of using four different sweeping methods to study the asymmetry problem can be observed. In figure 22(a), the phase envelope CEP was swept over. Comparing this to figure 22(d), where both the high- and low-frequency CEP was constant, it is clear that the impact from the CEP-change makes a difference. However, as figure 22(b)

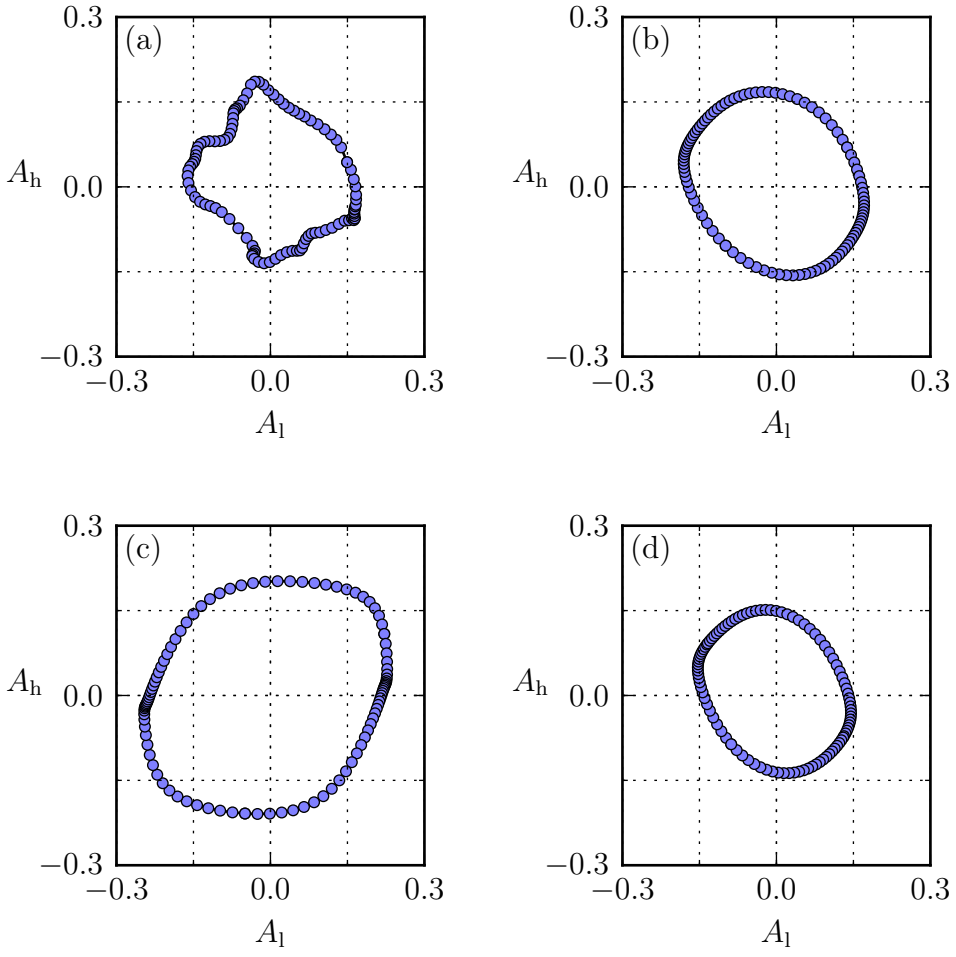

Figure 22: The $A_\mathrm{l} - A_\mathrm{h}$ representations of the 4136 division for different sweeping methods and I_rel of a two-colour field. In (a), the low-frequency field CEP was swept over in order to change the asymmetry, whereas in (b) and (c) the high frequency CEP was used. In (d) the origin point of the high frequency pulse was instead moved. In all images but (c), where $I_\mathrm{rel} = 0.15$, $I_\mathrm{rel} = 0.01$ was used.

and 22(c) shows, the high-frequency border effects are neither significant at $I_{\text{rel}} = 0.01$ nor $I_{\text{rel}} = 0.15$. Presumably the total effect of the border is greater in figure 22(c) than in 22(d), but also obscured by the much larger asymmetry effects due to the higher $I_{\text{rel}} = 0.15$.

Changing the CEP of either pulse changes the asymmetry in the same manner as changing ϕ. It is possible that the rough character of figure 22(a) is the result of a combination of positive and destructive interference between the two asymmetry contributions – sometimes both effects increase the number of electrons going in the positive z direction in the high-energy spectrum, sometimes one of them does the opposite. As expanded upon in section 3.7 below, however, this is not a sufficient explanation.

In figure 22(d), the length of the low-frequency pulse was the same as in the other subfigures, while the high-frequency pulse was contained within the low-frequency amplitude plateau, as explained in section 2.1.3. As expected, the total asymmetry of the pulse, and therefore the radius of the circle, decreased. This method is therefore clearly inferior to sweeping over the high-frequency CEP, which produces equally good results.

3.5 Pulse Envelope Shape

As can be seen in figure 23, a A_{l} – A_{h} representation like those created with trapezoidal $\omega - 2\omega$ pulses can be modelled with $\cos^2$ and Gaussian envelopes as well. This is relevant, as it shows that the phenomenon is not a result of the trapezoidal envelope shape.

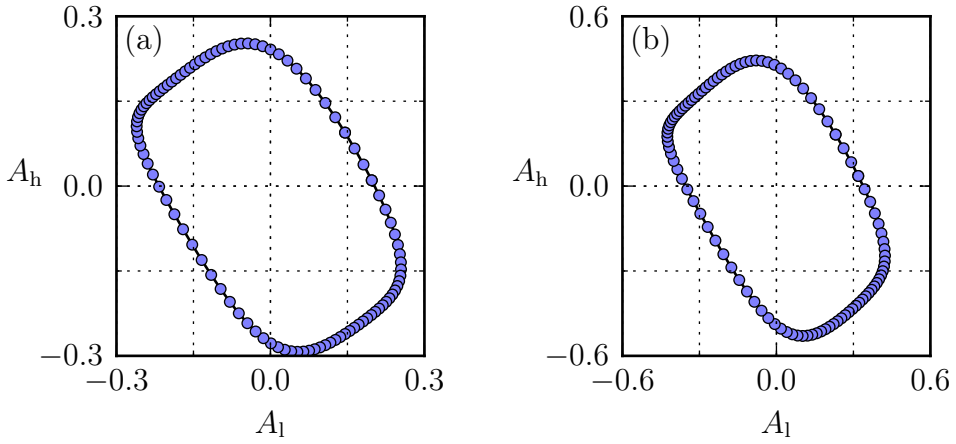

Figure 23: The A_{l} – A_{h} representations of the 4035 divisions of two two-colour pulses with $I_{\text{rel}} = 0.01$. In (a), a $\cos^2$ envelope was used, and in (b) a Gaussian.

3.6 System Dependence of Asymmetry

3.6.1 Relative Intensity

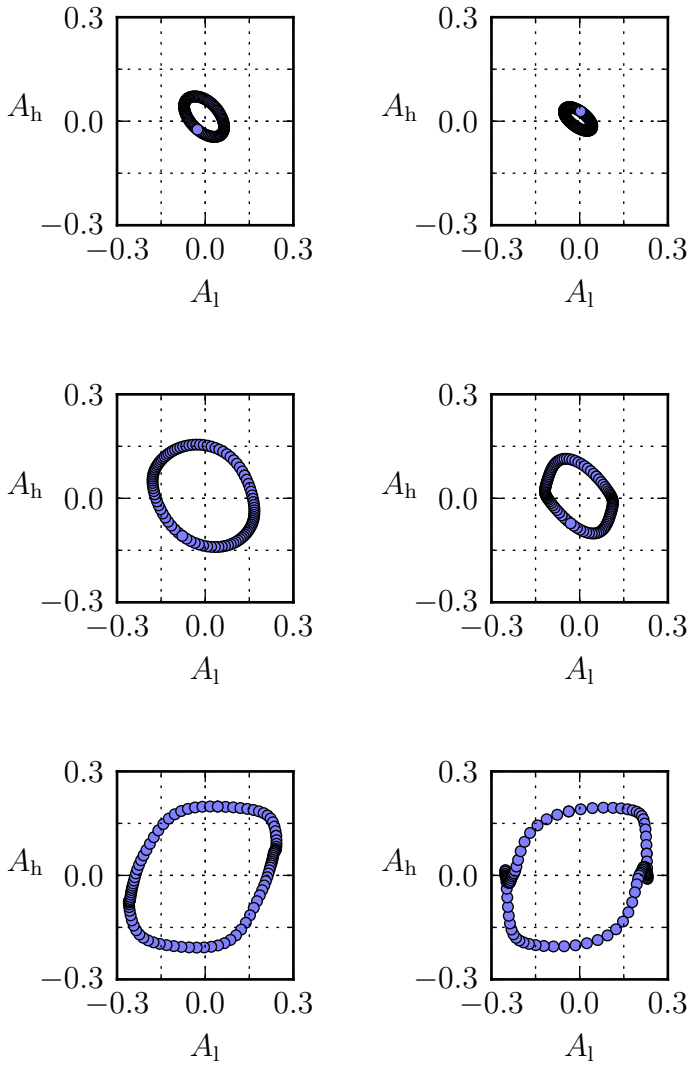

Figure 24: The upper and the lower rows give the 1137 and the 1216 divisions, respectively. The relative intensity was increased exponentially between the three columns, with a factor ≈ 12.5, so that $I_\mathrm{rel} \in \{0.001, 0.0125, 0.15\}$.

As can be seen in figure 24, the total asymmetry grows with I_{rel}. This is to be expected, as the high-frequency wave is the cause of the pulse asymmetry. What is not necessarily as obvious, however, is the possibility of a clear change of the shape of the asymmetry representation in the $A_{\text{l}} - A_{\text{h}}$ plane. For some divisions, such as 1216, $\theta\,(\phi)$ even stops being injective as I_{rel} increases, which can be seen in the right column of figure 24.

3.6.2 Wavelength

All previous figures were generated using $\lambda = 800$ nm. Figures 25 and 26 shows that the same process is applicable to other wavelengths.

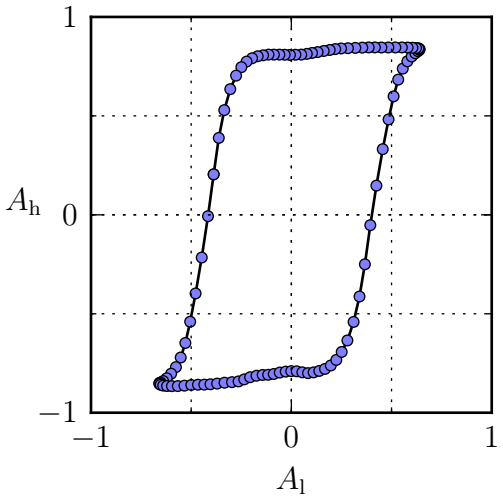

Figure 25: The 2012 division of a spectra generated with a high-intensity wavelength of 1300 nm and $I_{\text{rel}} = 0.1$.

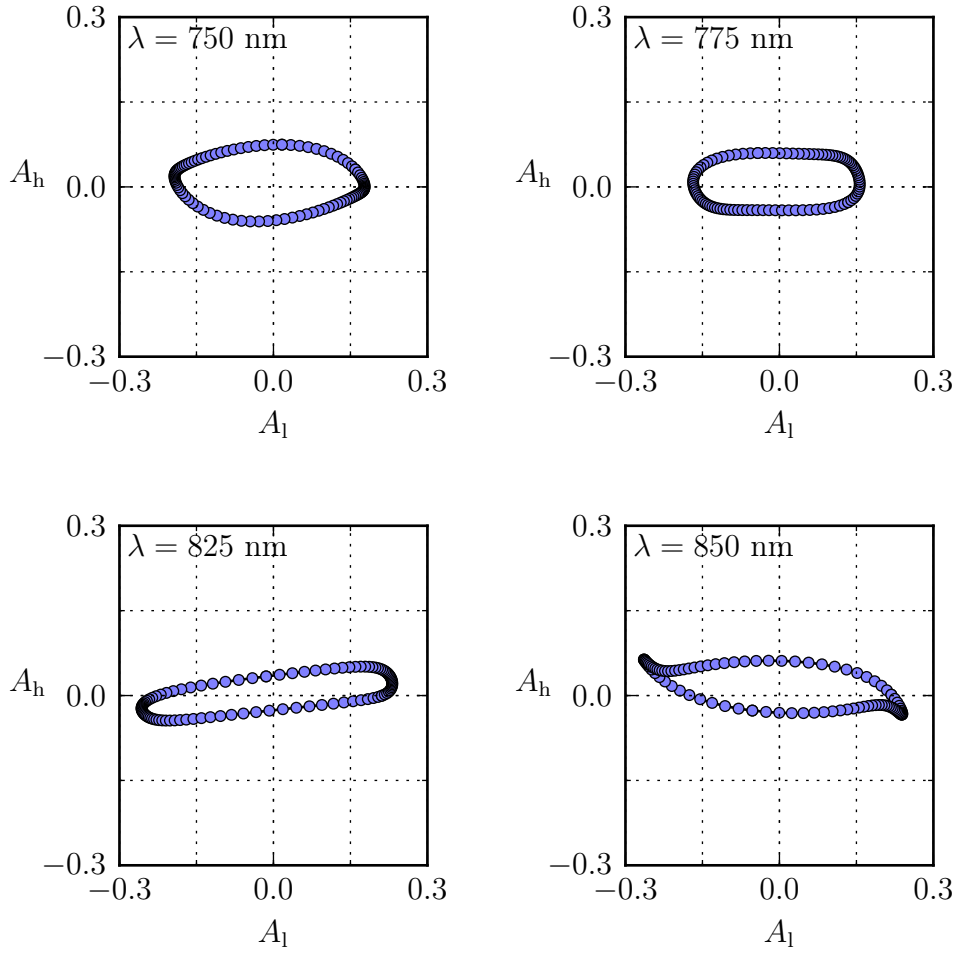

Figure 26: Different wavelengths can be used to generate asymmetry in the same manner as 800 nm was used to generate previous images.

3.7 Comparison with CEP for Short Pulses

In figure 27, the $A_\mathrm{l} - A_\mathrm{h}$ representations are shown for two short pulses. It illustrates the connection between the two-colour and the short-pulse cases. It can be noted that the shorter pulse, the $A_\mathrm{l} - A_\mathrm{h}$ representation of which can be found in figure 27(b), has a higher total asymmetry than the longer pulse, as seen in figure 27(a).

The short pulses' $A_\mathrm{l} - A_\mathrm{h}$ representations exhibit the same type of behaviour seen in figure 22(a). This indicates that this behaviour is intrinsic to CEP changes, rather than a result of interaction between the two contributions to asymmetry in figure 22(a), as put

forward as a possible explanation in section 3.4.

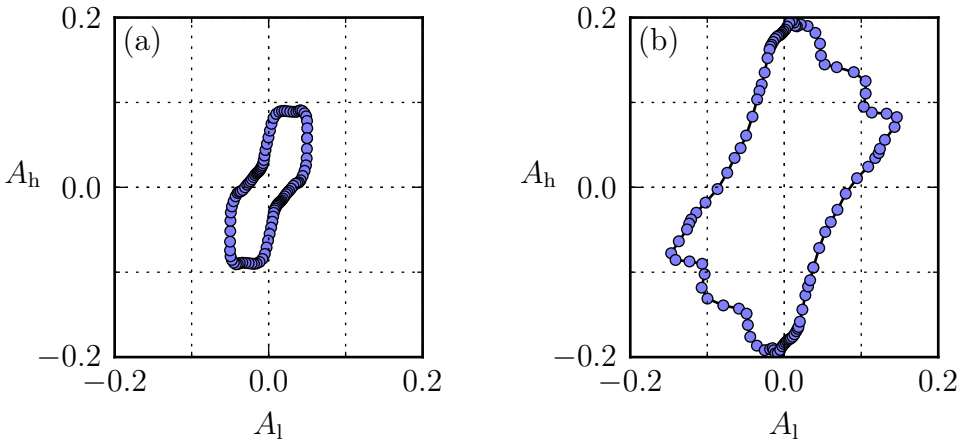

Figure 27: The $A_\mathrm{l} - A_\mathrm{h}$ representations of the 2719 division of two short pulses. The pulse CEP was changed in order to generate the different points on the circle. The pulses had $\cos^2$ envelopes, with a width of $\frac{8\pi}{\omega}$ for (a) and $\frac{16\pi}{\omega}$ for (b).

3.8 Odd Harmonics

In figure 28, ΔP, as defined in equation (30), is shown for several energies, as a function of ϕ'. The energy of the electrons ionised at $t_0 = \phi'$ is also shown. The largest electron yield occur when $\phi' \approx \frac{\pi}{2}$, with the exceptions of $\varepsilon \approx 10U_\mathrm{p}$ and $\varepsilon \approx 2U_\mathrm{p}$, $\phi' \approx \frac{\pi}{2}$. In other words, positive interference when the field strength, and therefore the ionisation rate, is already large, causes the highest ionisation rate.

The first exception is $\varepsilon = 10U_\mathrm{p}$. For this energy, the largest electron yield is given when ϕ' is slightly after the ionisation time which can cause $10U_\mathrm{p}$. As could be expected, the constructive interference increases the ionisation rate. It is possible that the ionisation rates for electrons observed with other energies mainly increase for $\phi' \approx \frac{\pi}{2}$, because the electrons can be ionised to those energies for several different t_0. The green and blue lines in figure 28 only show the maximum energy as a function of ionisation time, and while there is only one t_0 to yield $\varepsilon = 10U_\mathrm{p}$, there are many that can result in $6U_\mathrm{p}$. As t_0 becomes less important, the total ionisation rate becomes more important, and ϕ' goes to $\frac{\pi}{2}$.

The second exception is $\varepsilon = 2U_\mathrm{p}$. It is possible that same principle as for $10U_\mathrm{p}$ is in effect here, as far as only directly ionised electrons are considered, changing the center of mass of ΔP toward where $\varepsilon = 2U_\mathrm{p}$ for directly ionised electrons. While the rescattered electrons should even out the distribution slightly, they only make up a fraction of the total electron yield.

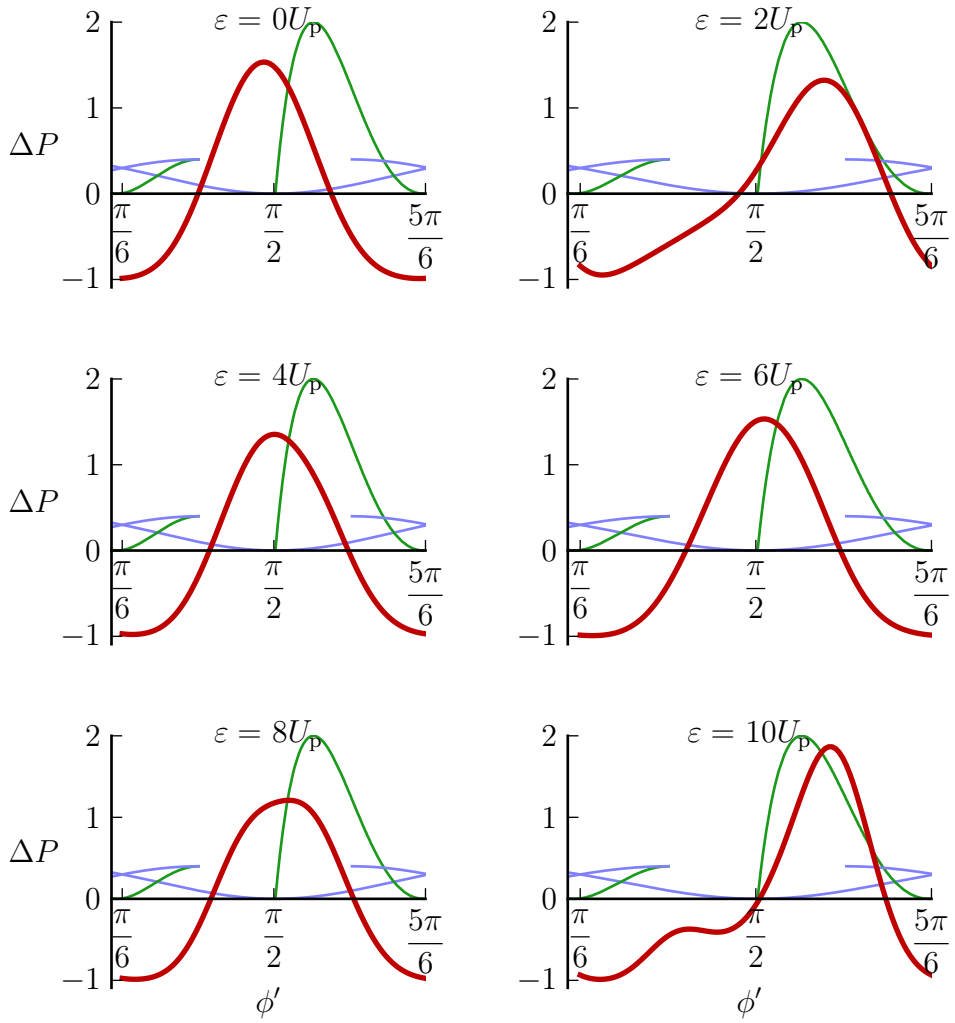

Figure 28: In red, the ϕ'-dependence of ΔP is shown. Despite ΔP seemingly extending to -1, which would represent a complete lack of ionisation, it is larger than -1 for all ϕ'. In blue the energies of the directly ionised, and in green the maximum energy of the rescattered, electrons freed at time $t_0 = \phi'$ is shown, the rescattered in green and the directly ionised in blue. The values of the energies are not given on the ordinate, but can be found in figure 3. For quick reference it can be noted that the maximum observed energies for directly ionised and rescattered electrons are $2U_\mathrm{p}$ and $10U_\mathrm{p}$, respectively. Also note that because the time between the peaks is shorter than half a cycle, the energy plot has been cropped and wrapped.

4 Conclusions

When initiating ATI using long, linearly polarised pulses, it is possible to control the appearance of the resulting electron spectrum by combining carrier waves with multiple frequencies. One such type of pulse is a two colour pulse, where one of the colours is a higher order harmonic of the other. By varying the relative intensity and the phase difference, ϕ, between the pulses, the character of the ATI spectrum will change.

For pulses where the higher harmonic is even, the ATI spectrum will display asymmetry between the positive and negative direction of the electric field. If an ATI spectrum has an overrepresentation of electrons over a certain energy interval, the spectrum in that region tends to go to being symmetrical, to being underrepresented in the aforementioned direction, to being symmetrical, and back to overrepresentation, when varying the phase difference a total of 2π. This symmetrical behaviour is a direct result of the shape of a two colour wave. It is possible to select two regions of the ATI spectrum, and by observing how the respective asymmetry of the regions depend on ϕ, gain a measure of ϕ.

When the relative intensity between the pulses increases, the total asymmetry of the spectrum also increases. However, it does not increase linearly and does not retain its general appearance. It is even possible for ϕ, when calculated from the measures used in this thesis, to loose its uniqueness for certain selections of regions in the energy spectrum.

As hinted on in the above paragraph, not all divisions of the energy spectrum are equally useful. It is possible to choose a division which, with a good degree of certainty, can give the approximate region of ϕ, and it is possible to select a division which produces a very accurate measure of ϕ, if the region is known.

If the harmonic is odd, the ATI spectrum will retain its symmetry. Instead the ionisation probability can be increased or decreased through constructive and destructive interference. For most energies, the ionisation potential increases the most when the peaks of the waves coincide, but the largest probability of ionisation for energies in the region of $2U_\mathrm{p}$ and $10U_\mathrm{p}$ will occur if there is constructive interference at times when the directly ionised electrons with energy $2U_\mathrm{p}$, and the rescattered electrons with energy $10U_\mathrm{p}$, respectively, are ionised.

References

[1] P. Agostini et al. "Free-Free Transitions Following Six-Photon Ionization of Xenon Atoms". In: *Physical Review Letters* 42 (17 Apr. 1979), pp. 1127–1130. DOI: 10.1103/PhysRevLett.42.1127. URL: http://link.aps.org/doi/10.1103/PhysRevLett.42.1127.

[2] W. Becker et al. "Above-threshold ionization: From classical features to quantum effects". In: *Advances in Atomic Molecular and Optical Physics* 48 (2002), pp. 35–98. DOI: 10.1016/S1049-250X(02)80006-4.

[3] G. G. Paulus, W. Becker, and H. Walther. "Classical rescattering effects in two-color above-threshold ionization". In: *Physical Review A* 52 (5 Nov. 1995), pp. 4043–4053. DOI: 10.1103/PhysRevA.52.4043. URL: http://link.aps.org/doi/10.1103/PhysRevA.52.4043.

[4] T. Wittmann et al. "Single-shot carrier-envelope phase measurement of few-cycle laser pulses". In: *Natyre Physics* 5.5 (May 2009), pp. 357–362. ISSN: 1745-2473. DOI: 10.1038/nphys1250. URL: http://dx.doi.org/10.1038/nphys1250.

[5] T Rathje et al. "Review of attosecond resolved measurement and control via carrier–envelope phase tagging with above-threshold ionization". In: *Journal of Physics B: Atomic, Molecular and Optical Physics* 45.7 (2012), p. 074003. DOI: 10.1088/0953-4075/45/7/07400. URL: http://stacks.iop.org/0953-4075/45/i=7/a=074003.

[6] Yi-Yian Yin et al. "Asymmetric photoelectron angular distributions from interfering photoionization processes". In: *Physical Review Letters* 69 (16 Oct. 1992), pp. 2353–2356. DOI: 10.1103/PhysRevLett.69.2353. URL: http://link.aps.org/doi/10.1103/PhysRevLett.69.2353.

[7] H. S. Nguyen, A. D. Bandrauk, and C. A. Ullrich. "Asymmetry of above-threshold ionization of metal clusters in two-color laser fields: A time-dependent density-functional study". In: *Physical Review A* 69 (6 June 2004), p. 063415. DOI: 10.1103/PhysRevA.69.063415. URL: http://link.aps.org/doi/10.1103/PhysRevA.69.063415.

[8] F. Brizuela et al. "Efficient high-order harmonic generation boosted by below-threshold harmonics". In: *Scientific Reports* 3 (2013). DOI: 10.1038/srep01410. URL: http://dx.doi.org/10.1038/srep01410.

[9] K. J. Schafer. "Strong Field Laser Physics". In: *Springer Series in Optical Sciences*. Ed. by T. Brabec. Vol. 134. Berlin: Springer, 2008.